Impact of Surface Roughness on AMSR-E Sea Ice Products

Julienne C. Stroeve, Thorsten Markus, *Member, IEEE*, James A. Maslanik, Donald J. Cavalieri, *Member, IEEE*, Albin J. Gasiewski, *Fellow, IEEE*, John F. Heinrichs, *Member, IEEE*, Jon Holmgren, Donald K. Perovich, and Matthew Sturm

***Abstract*—This paper examines the sensitivity of Advanced Microwave Scanning Radiometer (AMSR-E) brightness temperatures (Tbs) to surface roughness by a using radiative transfer model to simulate AMSR-E Tbs as a function of incidence angle at which the surface is viewed. The simulated Tbs are then used to examine the influence that surface roughness has on two operational sea ice algorithms, namely: 1) the National Aeronautics and Space Administration Team (NT) algorithm and 2) the enhanced NT algorithm, as well as the impact of roughness on the AMSR-E snow depth algorithm. Surface snow and ice data collected during the AMSR-Ice03 field campaign held in March 2003 near Barrow, AK, were used to force the radiative transfer model, and resultant modeled Tbs are compared with airborne passive microwave observations from the Polarimetric Scanning Radiometer. Results indicate that passive microwave Tbs are very sensitive even to small variations in incidence angle, which can cause either an over- or underestimation of the true amount of sea ice in the pixel area viewed. For example, this paper showed that if the sea ice areas modeled in this paper were assumed to be completely smooth, sea ice concentrations were underestimated by nearly 14% using the NT sea ice algorithm and by 7% using the enhanced NT algorithm. A comparison of polarization ratios (PRs) at 10.7, 18.7, and 37 GHz indicates that each channel responds to different degrees of surface roughness and suggests that the PR at 10.7 GHz can be useful for identifying locations of heavily ridged or rubbled ice. Using the PR at 10.7 GHz to derive an "effective" viewing angle, which is used as a proxy for surface roughness, resulted in more accurate retrievals of sea ice concentration for both algorithms. The AMSR-E snow depth algorithm was found to be extremely sensitive to instrument calibration and sensor viewing angle, and it is concluded that more work is needed to investigate the sensitivity of the gradient ratio at 37 and 18.7 GHz to these factors to improve snow depth retrievals from spaceborne passive microwave sensors.**

***Index Terms*—Passive microwave, remote sensing, sea ice.**

Manuscript received December 1, 2005; revised March 24, 2006. This work was supported by the National Aeronautics and Space Administration under Grants NNG04GH68G and NAG5-11369.

J. C. Stroeve is with the National Snow and Ice Data Center, Cooperative Institute for Research in Environmental Sciences, University of Colorado at Boulder, Boulder, CO 80309 USA (e-mail: stroeve@kodiak.colorado.edu).

T. Markus and D. J. Cavalieri are with the National Aeronautics and Space Administration-Goddard Space Flight Center, Greenbelt, MD 20771 USA.

J. A. Maslanik is with the Colorado Center for Astrodynamics Research, University of Colorado at Boulder, Boulder, CO 80309 USA.

A. J. Gasiewski is with the Department of Electrical and Computer Engineering, University of Colorado, Boulder, CO 80309 USA.

J. F. Heinrichs is with the Department of Geosciences, Fort Hays State University, Hays, KS 67601 USA.

J. Holmgren and M. Sturm are with the U.S. Army Cold Regions Research and Engineering Laboratory-Alaska, Fort Wainwright, AK 99703 USA.

D. K. Perovich is with the U.S. Army Cold Regions Research and Engineering Laboratory, Hanover, NH 03755 USA.

Digital Object Identifier 10.1109/TGRS.2006.880619

I. Introduction

OBSERVATIONS from successive multichannel passive microwave satellite sensors provide nearly 30 years of sea ice observations for the Arctic and Antarctic. Data from passive microwave radiometers first became available in December 1972 from the Nimbus-5 Electrically Scanning Microwave Radiometer (ESMR). However, it was not until 1978, with the launch of the Nimbus-7 Scanning Multichannel Microwave Radiometer (SMMR), that the polar regions became routinely observed using multichannel passive microwave sensors. SMMR was followed by a series of successive Defense Meteorological Satellite Program (DMSP) Special Sensor Microwave/Imager (SSM/I) sensors in 1987. The Advanced Microwave Scanning Radiometer (AMSR-E) continues this relatively long history of polar remote sensing.

Several algorithms have been developed to estimate the fraction of sea ice in the polar oceans from satellite passive microwave observations (e.g., [3], [4], [10], and [13]). Analysis of sea ice extent using the National Aeronautics and Space Administration (NASA) Team (NT) sea ice algorithm [2], [3] has shown that Arctic sea ice has rapidly declined since the late 1970s [16]. However, to make these types of assessments, consistent data sets from similar sensors on successive spacecraft are needed. This requires understanding differences in ice concentration estimates from similar sensors as well as understanding differences resulting from changes in sea ice algorithms. In an earlier paper, differences in ice concentrations and ice extent between successive SSM/I instruments were documented [17]. Although the sea ice algorithm was consistent between the sensors, this paper showed that significant regional differences in ice concentrations and ice extent exist between the different SSM/Is (e.g., F8, F11, and F13) and revealed that earlier efforts to match orbital antenna temperatures or gridded brightness temperatures (Tbs) between different sensors were insufficient to remove regional biases in Tbs and subsequently in the derived sea ice concentrations. The approach taken by Cavalieri *et al.* [2] is to tune the algorithm tie points (reference Tbs) for each sensor to minimize differences in ice extent during sensor overlap periods. However, despite this approach, regional biases in ice concentration remain.

Improved polar ocean products are expected from AMSR-E because of additional spectral channels, greater spatial resolution, and enhanced system performance. The AMSR-E sea ice algorithm uses a revised version of the NT algorithm, which is referred here as the NT2 algorithm, to retrieve the total fraction of sea ice per pixel [10]. In addition, snow depth over seasonal ice is retrieved using the snow depth algorithm of Markus and

Cavalieri [11] applied to the AMSR-E Tbs. Using AMSR-E to extend the sea ice extent/concentration time series provided by SMMR and SSM/I will require quantifying the differences in ice concentration induced not only by the use of a different sensor but also by the use of a different sea ice algorithm. We can expect considerable and essentially unexplained differences to exist in ice concentrations produced by the NT2 and NT algorithms. Ice concentration variations may result from the use of different sets of channels in the algorithms; different responses to changes in atmospheric conditions, surface temperatures, and emissivities; different algorithm tie points; and differences in the ways that the tie points are selected [13]. Radiative transfer modeling (RTM) sensitivity experiments (not shown) suggest that differences may also result from the ways in which the algorithms respond to variations in snowpack conditions such as depth hoar, snow depth/density, ice lenses, and flooding at the snow/ice interface.

Whereas the NT2 algorithm incorporates an RTM component (as part of the atmospheric correction step), the standard validation plan does not use RTM as a validation tool. Such modeling is an integral part of a number of other AMSR product validation efforts. The use of an RTM approach that combines sea ice and atmospheric components to simulate radiances at AMSR-E frequencies allows for the opportunity to extend subjective comparisons between algorithms and sensors and assess the degree to which observed differences can be attributed to surface and/or atmospheric conditions.

Therefore, to improve our understanding of differences in ice concentrations resulting from changes in sea ice algorithms as well as changes in sensors, a modeling approach is used. Two different types of models were used for this effort, namely: 1) the Microwave Emission Model of Layered Snowpacks (MEMLS) [21] and 2) the MicroWave MODel (MWMOD) [6]. MEMLS is a thermal microwave emission model and is based on radiative transfer, taking multiple-volume scattering and absorption into account. Since microwave scattering efficiency depends upon snowpack properties, the model accounts for parameters such as grain size, density, temperature, and liquid water content. MWMOD is an emission model developed for use with a layered sea ice column and snow cover and includes an atmospheric model. Powell *et al.* [12] discuss the MEMLS model in more detail and investigates the response of snow physical properties and snow layering on AMSR-E Tbs using MEMLS. Two unanswered questions remain, however. One is the effect of the emissivity of the underlying sea ice, and the other is the impact of surface roughness. In this paper, we investigate how observed variations in Tbs obtained during a field campaign in March 2003 near Barrow, AK, can be explained by variations in surface roughness using model calculations from MWMOD. This effort will help to assess the role that roughness plays in ice concentration and snow depth retrieval algorithms.

II. Methodology

The modeling approach is based on a combination of RTM in conjunction with use of comprehensive *in situ* data obtained at individual stake locations made along transects on Elson Lagoon, the Beaufort Sea, and the Chukchi Sea. These detailed measurements made at discrete stake locations are unique, as they provide several of the necessary parameters required as input into a combined sea ice/snow/atmospheric model (e.g., MWMOD). The inputs include snow depth, snow grain size, snow stratigraphy (including hoar fraction), snow water equivalent, snow/ice interface salinity, surface temperature, snow/ice interface temperature, 10-cm-deep ice temperature, and ice thickness. The simulated Tbs are compared with passive microwave observations from aircraft and used as input to the NT and NT2 sea ice algorithms to examine the effects of roughness on algorithm output.

A. Field Data

In March 2003, a field campaign was conducted near Barrow, AK. The primary objective of the field campaign was to validate sea ice products from AMSR-E, including ice concentration, snow depth, and ice temperature, through the collection of sea ice and snow properties on the sea ice near Barrow, AK. *In situ* and aircraft measurements were made over Elson Lagoon, the Beaufort Sea, and the Chukchi Sea (Fig. 1). Elson Lagoon is protected by barrier islands and consisted of smooth first-year ice (FYI) with moderate snow drifts (< 60 cm). Similar ice conditions were found near the shore of the Chukchi Sea, although this ice was thinner and younger than the Elson ice. The area of the Beaufort Sea sampled also consisted of FYI, but this ice had undergone moderate (< 1 m) to heavy (> 5 m) ridging. Consequently, this area had rough surface topography compared to the Elson Lagoon and Chukchi Sea areas sampled and exhibited a wide range of snow conditions that included areas of little or no snow to snow drifts deeper than 1 m. An additional validation site was the Navy Ice Camp (72°55′ N, 147°34′ W), which is situated about 175 km northeast of Barrow and contained a mixture of FYI and multiyear ice (MYI) floes with moderate ridging.

On March 13, coincident aircraft (NASA P-3) Polarimetric Scanning Radiometer (PSR) and *in situ* snow and ice measurements were made [1]. Details of the field experiment, including a summary of all *in situ* measurements made, can be found in [18]. Measurements of snow depth, ice thickness, temperature, and detailed snow pit measurements at discrete locations from March 13 obtained from the Elson Lagoon transect and extended part ways into the Beaufort Sea are used as input into MWMOD as described in the next section to simulate the observed PSR Tbs. Figs. 2 and 3 show snow depth and ice thickness variability, respectively, along the Elson/Beaufort transect shown by the green line in Fig. 1. Mean snow depth for the Elson Lagoon area sampled was 13.7 cm ($\pm$8.80 cm), whereas that for the Beaufort area sampled was 18.2 cm ($\pm$16.18 cm). Locations where in-depth snow pit measurements were made at discrete stake locations are shown along the x axis in Fig. 2 as black squares. Snow pit measurements consisted of snow depth, density, snow water equivalent, stratigraphy (including hoar fraction), snow grain size, salinity, and temperature at the snow surface, snow/ice interface, and 10 cm below the ice. These data are used as input into MWMOD to simulate the PSR Tbs at each stake location.

B. Aircraft PSR Data

Two PSR transects were flown at 500 ft. At this altitude, the PSR was operated in stare mode, which means that the PSR is not conically scanning but is operating at a fixed beam position,

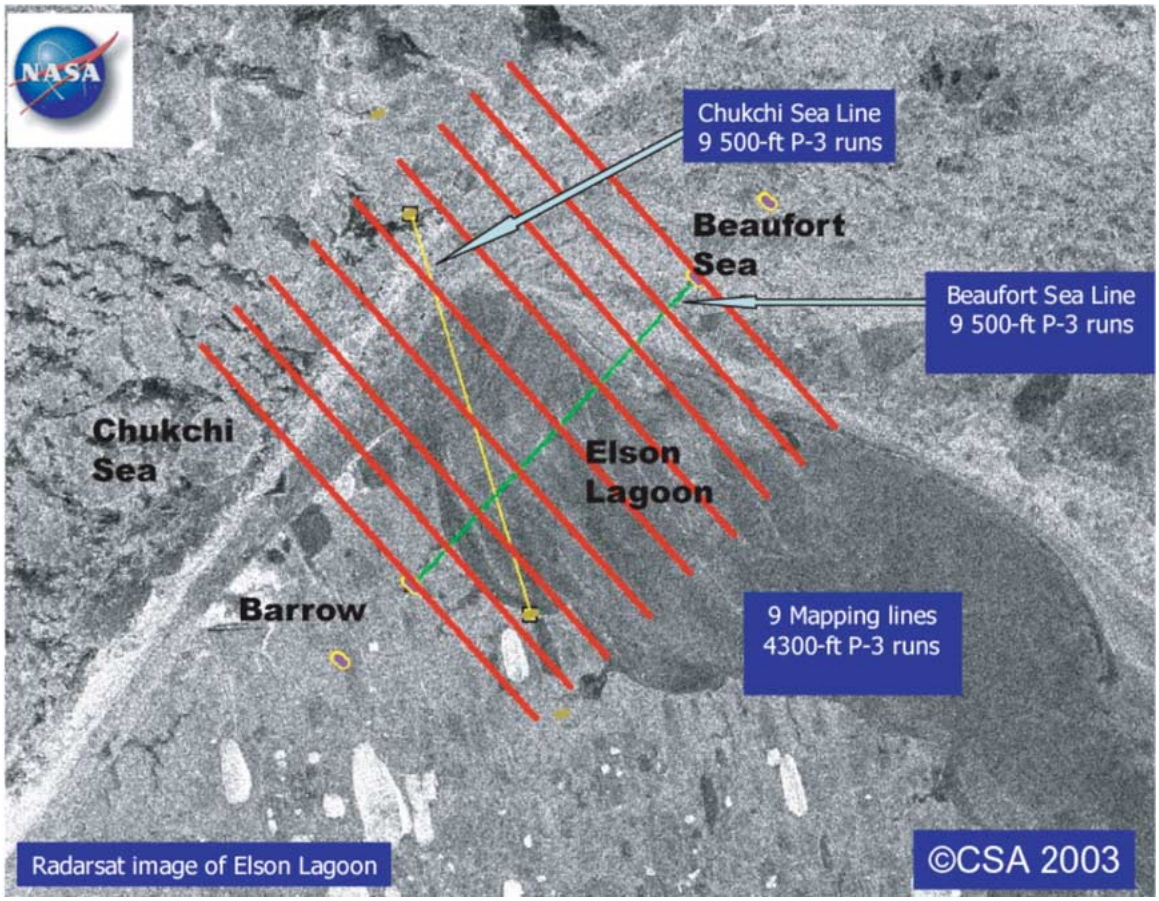

Fig. 1. Site map of the Barrow study area. Place names, surface transects, and NASA P-3 aircraft flight lines are shown superimposed on a RADARSAT synthetic aperture radar (SAR) image. The Elson transect is shown in green. The Chukchi transect is shown in yellow. Note the relatively even texture of the Elson Lagoon ice (indicating relatively smooth ice) compared to the variability in ice conditions apparent along the Chukchi Sea coastline and offshore of the barrier islands enclosing Elson Lagoon to the north.

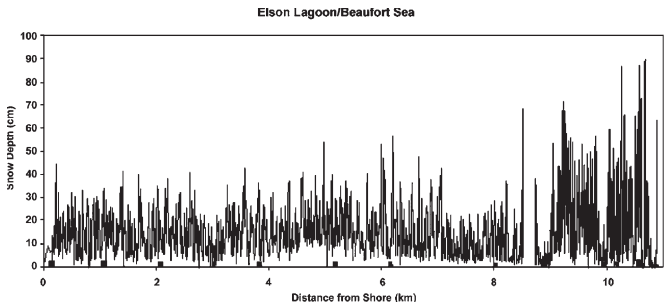

Fig. 2. Beaufort Line shown in Fig. 1. The gap between 8 and 9 km occurs at the barrier island between Elson Lagoon and the Beaufort Sea. Locations of individual stake locations where in-depth snow pit measurements were made are shown along the x axis by black squares.

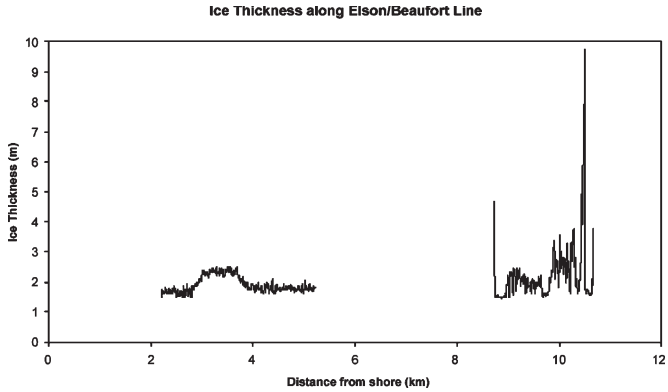

Fig. 3. Ice thickness from electromagnetic (EM-31) observations for 1000 data points along the Elson Lagoon/Beaufort line shown in Fig. 1. The thick ice on the Beaufort transect maps directly onto a big ridge. EM-31 is accurate up to 6 m, so it is unclear if the ridge is 7–9 m thick or 6.5–8 m thick.

i.e., pointing at 55°. However, this angle varied somewhat because the aircraft had to adjust for wind, etc. The spatial resolution of the PSR measurements at this altitude is about 30 m. Because of geolocation inaccuracies and corrections for aircraft drift, the transects were overflown several times to ensure good spatial agreement between the aircraft observations and the ground measurements. Additionally, the area was covered at higher altitude (4500 ft) with the PSR operating in scan mode to cover a wider region so that findings from low-altitude flights could be extrapolated to a larger area. For high-altitude flights, the PSR spatial resolution is about 500 m.

The PSR data collected at an altitude of 500 ft are used in the comparisons with model simulations. The data collected at an altitude 4500 ft are used to calibrate the PSR data relative to AMSR-E as discussed below. A more detailed description of the calibration method can be found in [9].

Initial analysis of the PSR data indicated problems with instrument calibration. PSR Tbs were compared with coincident AMSR-E Tbs over the marginal sea ice zone and covered a wide range of expected Tbs from open water to consolidated sea ice.

The comparison was used to examine the agreement in calibration between the two data sets and ensure that AMSR-E sea ice concentration and snow depth algorithm coefficients could be applied to the PSR data. Results showed overall good linear correlation between the two sensors for the lower frequency channels (see [9]). The 89-GHz Tbs, however, exhibited large differences between the two sensors and significant scatter. The scatter and offset at 89 GHz could not be explained by differences in footprint size between the AMSR-E and PSR observations. One explanation examined was the influence of atmospheric effects. Atmospheric radiative transfer calculations for a clear winter atmosphere show differences between PSR and AMSR-E Tbs ranging from $\sim$0.5 K at 6 GHz to 3 K at 89 GHz. These differences are too small, however, to explain the observed Tb differences between the two sensors, except at 18- and 37-GHz vertical polarization. There also appeared to be a continuous shift in calibration differences, with the difference between AMSR-E and PSR Tbs decreasing with increasing frequency, except at 89 GHz. To evaluate sea ice concentration and snow depth algorithm dependencies on surface roughness, PSR Tbs were regressed toward AMSR-E so that the AMSR-E algorithm coefficients would be applicable to the PSR data. For the regression, only the end points of the distribution in Tbs (e.g., pure open water and pure consolidated sea ice) were used to determine the appropriate slopes and offsets for each channel. Since the 89-GHz channels exhibited large unexplained variability, they could not be calibrated using this method. This was unfortunate, as the 89-GHz channels play a crucial role in the NT2 algorithm.

It is important to remember that the calibration process applied to the lower frequency PSR channels as described earlier does not remove all uncertainty in the PSR data. Geolocation errors remain a factor. Fig. 4(a) and (b) shows examples of variability in PSR Tbs at two stake locations, i.e., at 5.20 km (Elson Lagoon) and 9.97 km (Beaufort Sea). The PSR Tbs are plotted as a function of distance from the stake location (up to 100 m) for both flight directions. Geolocation error likely contributes a large part of the significant directional variability in Tbs at both polarizations at the stake locations shown. Variability in surface properties is also expected to contribute to the spatial variability seen in Fig. 4(a) and (b). The variability is most pronounced for the 89-GHz channel. Less spatial and directional variability is generally observed at lower frequencies, although this is not always the case, particularly at horizontal polarizations that are more sensitive to surface properties than vertical polarizations. However, since lower frequency channels have a larger penetration depth, we would expect less variability than that observed at 89 GHz.

C. Model Description

The MWMOD sea ice/atmospheric model [6] is designed to compute Tbs from 1 to 100 GHz, including sea ice, open ocean, and atmosphere, using the multilayer strong fluctuation theory (SFT) presented in [15]. The SFT model is a volume scattering model that uses the random medium approach. This model treats the interference between waves reflected and transmitted through the various layer planar interfaces coherently. Emissivities are computed based on Kirchoff's law, which relates emissivity to reflectivity. The model describes the emissivity of isothermal layers of snow and ice that are defined by temperature, thickness, density, salinity, diameter of air bubbles, ice and snow grains, liquid water content, angle of brine pockets, and the ratio of the length to the width of the brine pockets. More detail is given in [14] and [15].

The model for the atmosphere is described by the radiative transfer equation and solved using the "successive order of scattering" method. The gaseous absorption of oxygen and water vapor in the atmosphere is calculated with the millimeter-wave propagation model in [8]. Attenuation by clouds and precipitation are modeled by Mie theory. The radiative coupling to the surface, open, or ice-covered ocean is accomplished by reflectivities and emission temperatures supplied by the corresponding surface models.

Table I compares several MWMOD-derived emissivities of sea ice with observed values given in [5] and [20]. Where available, standard deviations of the observations are given in parentheses. The open-water emissivities were computed assuming a sea surface temperature (SST) of 272.39 K, salinity of 33%, and a wind speed of 6 ms^{-1} and compare well with the values given in [5]. For the different ice types modeled, information on ice/snow properties came from [20]. Good agreement is also found for the thin-ice case without snow cover. Larger differences occur between observed and modeled emissivities for FYI and MYI. The dominant factor that contributes to the variability of the FYI and MYI signatures modeled here is snow cover. The thickness and density of the highly porous surface layer of the MYI can also be a significant factor. This makes it difficult to compare modeled FYI and MYI signatures with observations since detailed information on the surface conditions when the observations were made is not available.

More extensive validation of MWMOD has been performed in [6] by comparing modeled Tbs with SSM/I data. Their results showed large deviations for the 37-GHz channels over sea ice (not over open ocean), whereas the simulated Tbs for the other channels were within the acceptable range. This paper concluded that the source for the large deviations at 37 GHz over sea ice is likely a result of the absence of a surface scatterer in the model. However, Table I shows generally better agreement with observations at 37 GHz than at lower frequency channels. The same result was found in this paper when simulating PSR Tbs (see the next section).

It is important to note that discrepancies between modeled and observed Tbs likely also result from how the model treats interactions between waves scattered or reflected. SFT models treat the interactions of the scattered and reflected waves coherently, and thus, the waves interfere. This is valid when layer interfaces are nearly planar (measured in radiation wavelengths), and the scattering in the layers is not too strong. However, since microwave signatures are very sensitive to this interference, they are highly dependent upon layer thickness, radiation wavelength, and incidence angle and therefore show strong oscillations with frequency and thickness. An example of this feature is shown in Fig. 5 where the dependence of the Tbs at 10.7 and 37 GHz to small changes in snow depth over thick MYI ice is plotted. At horizontal polarizations, large oscillations in the Tbs are found as a function of the top layer snow thickness. In general, these oscillations are reduced in sea ice because of the large variations in ice thickness and snow depth within the footprint of aircraft or satellite radiometers. These oscillations can be averaged out by varying the ice/snow

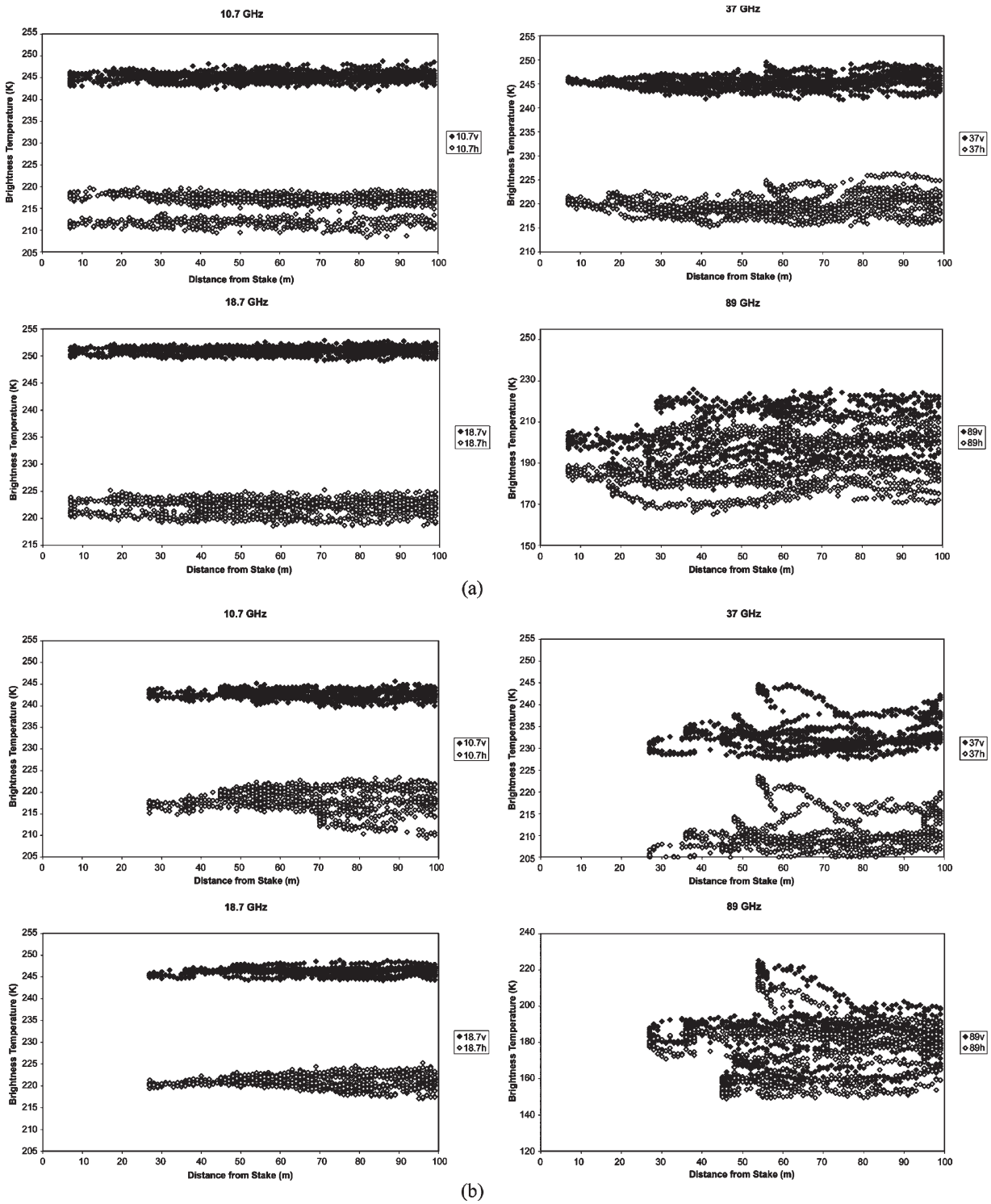

Fig. 4. (a) PSR brightness temperature variation at stake 5.20 km on Elson Lagoon. (b) PSR brightness temperature variation at stake 9.97 km on Beaufort Sea. For (a) and (b), note the large variability in Tbs, especially at horizontal polarizations and at 89 GHz. The variability is more pronounced over the rougher Beaufort ice than the smooth ice observed over Elson Lagoon in (a).

thickness over a small range of thicknesses [14]. Since the comparisons made by [6] were made using unaveraged MWMOD-derived Tbs, caution is needed when interpreting their results since some of the observed model differences are often the same magnitude as the oscillations themselves.

For our purposes, we can maximize the performance of MWMOD by using the averaging method noted earlier to obtain more realistic solutions that represent a surface consisting of moderate variations in snow depth. At the same time, we recognize that ongoing research seeks to address the shortcomings of the surface scattering model, and some alternatives currently exist that might provide improvement for simulating the effects of volume scattering. Fig. 6 shows results using this averaging method, at 18.7 (top) and 37 GHz (bottom) as a

TABLE I
COMPARISON BETWEEN MODELED AND MEASURED EMISSIVITIES FOR VARIOUS SURFACE TYPES. MODELED EMISSIVITIES ARE SHADED IN GRAY. STANDARD DEVIATIONS OF THE OBSERVED EMISSIVITIES ARE GIVEN INSIDE PARENTHESES

Ice Type/Source	Pol	6.7	10.0	18.7	21	37	90
Open Water [5]	V	0.513 (0.015)	0.532 (0.015)	0.570 (0.033)	0.617 (0.015)	0.662 (0.029)	0.792 (0.019)
	H		0.295 (0.020)	0.332 (0.018)	0.332 (0.018)	0.392 (0.015)	0.528 (0.022)
Model Simulation	V	0.514	0.534	0.592	0.617	0.689	0.812
	H	0.268	0.287	0.325	0.339	0.402	0.539
Thin Ice w/o snow [20]	V	0.98 (0.01)	0.93 (0.01)	0.97 (0.01)		0.96 (0.01)	0.95 (0.01)
	H	0.93 (0.02)	0.70 (0.02)	0.78 (0.02)		0.82 (0.02)	0.85 (0.02)
Model Simulation	V	0.981	0.970	0.983	0.983	0.971	0.983
	H	0.854	0.773	0.805	0.808	0.817	0.813
FYI [20]	V	0.900 (0.020)	0.924 (0.036)	0.941 (0.019)	0.960 (0.019)	0.955 (0.015)	0.926 (0.045)
	H	0.850 (0.065)	0.840 (0.025)	0.876 (0.021)	0.910 (0.020)	0.913 (0.013)	0.886 (0.031)
Model Simulation	V	0.983	0.989	0.991	0.986	0.981	0.998
	H	0.847	0.878	0.937	0.944	0.948	0.997
MYI [20]	V	0.96 (0.01)	0.92 (0.01)	0.81 (0.01)		0.75 (0.01)	0.71 (0.01)
	H	0.95 (0.02)	0.90 (0.02)	0.72 (0.02)		0.75 (0.02)	0.68 (0.02)
Model Simulation	V	0.98	0.96	0.88		0.88	0.77
	H	0.92	0.94	0.83		0.80	0.83

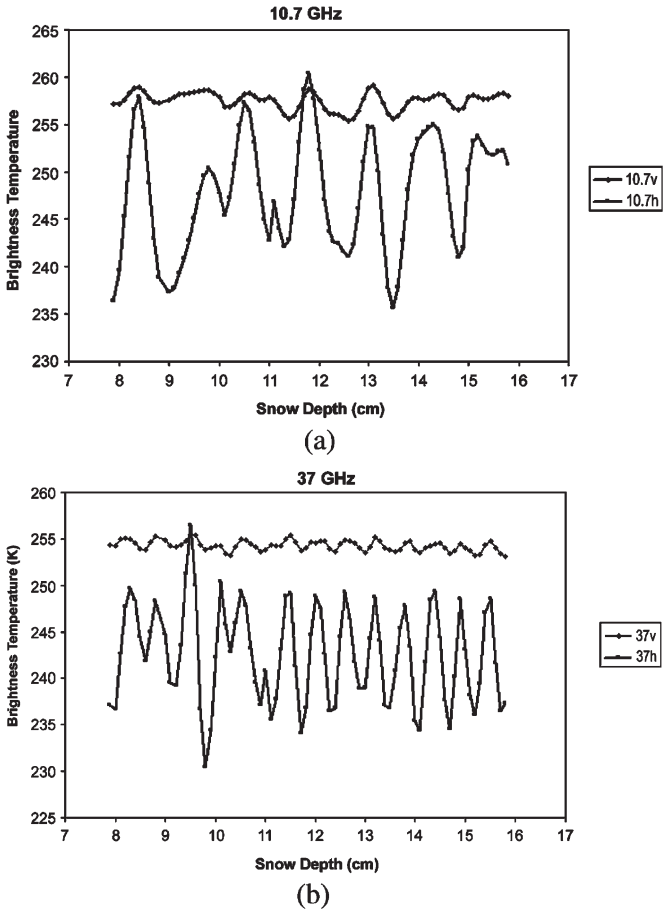

Fig. 5. (a) Variation of modeled brightness temperature at 10.7 GHz as a function of snow depth over thick MYI. Snow depth ranges from 8–16 cm. (b) Variation of modeled brightness temperature at 37 GHz as a function of snow depth over thick MYI. Snow depth ranges from 8–16 cm.

function of sensor incidence angle along with observations for a thin (8 cm) snow-free gray ice sheet that was grown as part of the 1988 Cold Regions Research and Engineering Laboratory Experiment (CRRELEX) and is thought to be similar to ice in stationary Arctic leads. To simulate this ice type, we modeled the sea ice using eight layers of equal thickness (1 cm). Inputs included a linear temperature profile, with a value of $-16\ ^{\circ}\mathrm{C}$ at the air/ice interface and a temperature of $-2\ ^{\circ}\mathrm{C}$ at the ice/water interface and measured inputs of salinity. Information on ice density, air bubble diameter, brine pocket angle, and ratio of the length and radius of the brine pockets was not known for the case study. Mean brine pocket tilt and brine pocket length to width were set to values suggested by previous characterization studies of artificial sea ice in CRRELEX. Specifically, these values are 4° for the mean brine pocket tilt (from vertical) and 10 for the ratio of brine pocket length to width (versus a tilt of 24° and a ratio of 200 used in [15]) and were assumed not to vary with depth. Air pockets in the model are assumed to occur only between the ice grains, so that the ice grains consist of brine and ice. The diameter of the air pockets (bubbles) is set to 1.0 mm throughout the ice sheet, which is similar to the values used in [6]. Ice grain sizes are typically several millimeters. For the ice grain size profile in this simulation, the first two layers are set to a value of 0.5 mm. The next two layers are set to a grain size of 1.0 mm, and the remaining layers have an ice grain size of 10 mm. Ice density is assumed to vary between 0.90 and $0.93\ \mathrm{g \cdot cm^{-3}}$. Sensitivity studies (not shown) show that for this ice type, the emissivity showed little dependence on variations in the top layer ice grain size.

Results are shown as a function of incidence angle to highlight the dependency of the emissivity on incidence angle, which will be discussed in more detail later. Because the reflectivity increases with incidence angle, we see a rapid decrease in the emissivity as the observation goes toward 90°. Between 50° and 60°, the emissivity predictions at 18.7 and 37 GHz differ from observations by less than 0.02 and are seen to be sensitive to small changes in sensor incidence angle such as that observed between SMMR, SSM/I, and AMSR. This sensitivity results in a decrease in the total ice fraction derived from the NT algorithm at a rate of 2% (absolute) per 1° change in sensor

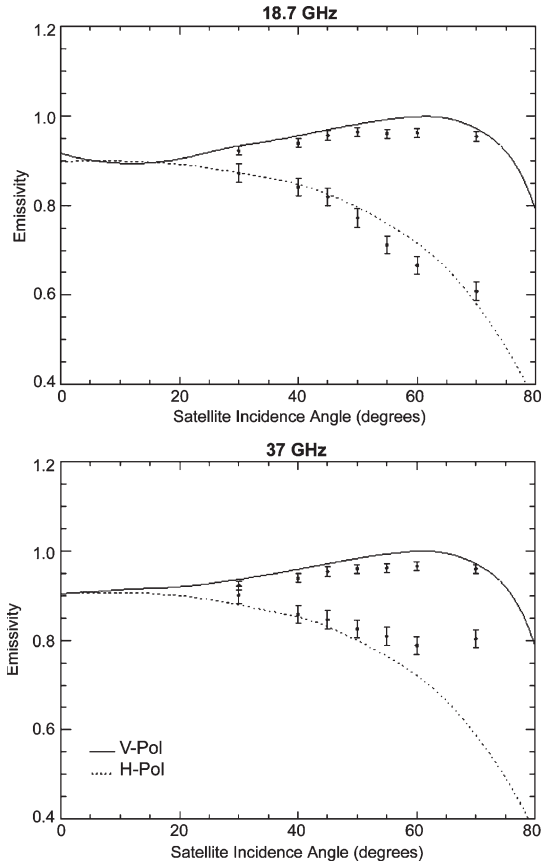

Fig. 6. Modeled and observed (plus standard deviation) emissivity at 18.7 and 37 GHz as a function of incidence angle for a thin (8 cm) snow-free ice sheet. The model was run assuming no overlying atmosphere for the comparisons. However, the resulting brightness temperatures (and emissivities) do not correspond exactly to measurements for downward-looking radiometers positioned on the ice because space background radiation is reflected at the ice/ocean surface. Even when the emissivity of the ice is very high, the contribution of the reflected radiance is small, but not negligible. Note further that MWMOD computes brightness temperatures at certain discrete incidence angles (i.e., we choose the maximum of 12 angles) that do not directly correspond to the results given in [20], and therefore, the emissivities were interpolated to give values at other incidence angles.

viewing angle between 50° and 60°. Thus, differences in the SMMR (50°), SSM/I ($\sim 53°$), and AMSR (55°) viewing angles result in differences as large as 10% (absolute) in the total ice fraction for this ice type. For thicker sea ice with snow cover, the modeled emissivity (not shown) shows less dependence on sensor viewing angle, resulting in differences in total ice fraction between 2% and 5% between the sensors.

III. Results

A. Model Simulations

Fig. 7 and Table II compare modeled and observed Tbs at each stake location using the comprehensive data collected from snow pits to simulate the snow/ice surface. As discussed previously for the CRRELEX thin-ice case study, assumptions were made regarding variables that are unknown such as ice salinity profile, diameter of air bubbles in the ice, and ice grain size as well as the tilt of the brine pockets and the ratio of the brine pocket length to width in the model simulations.

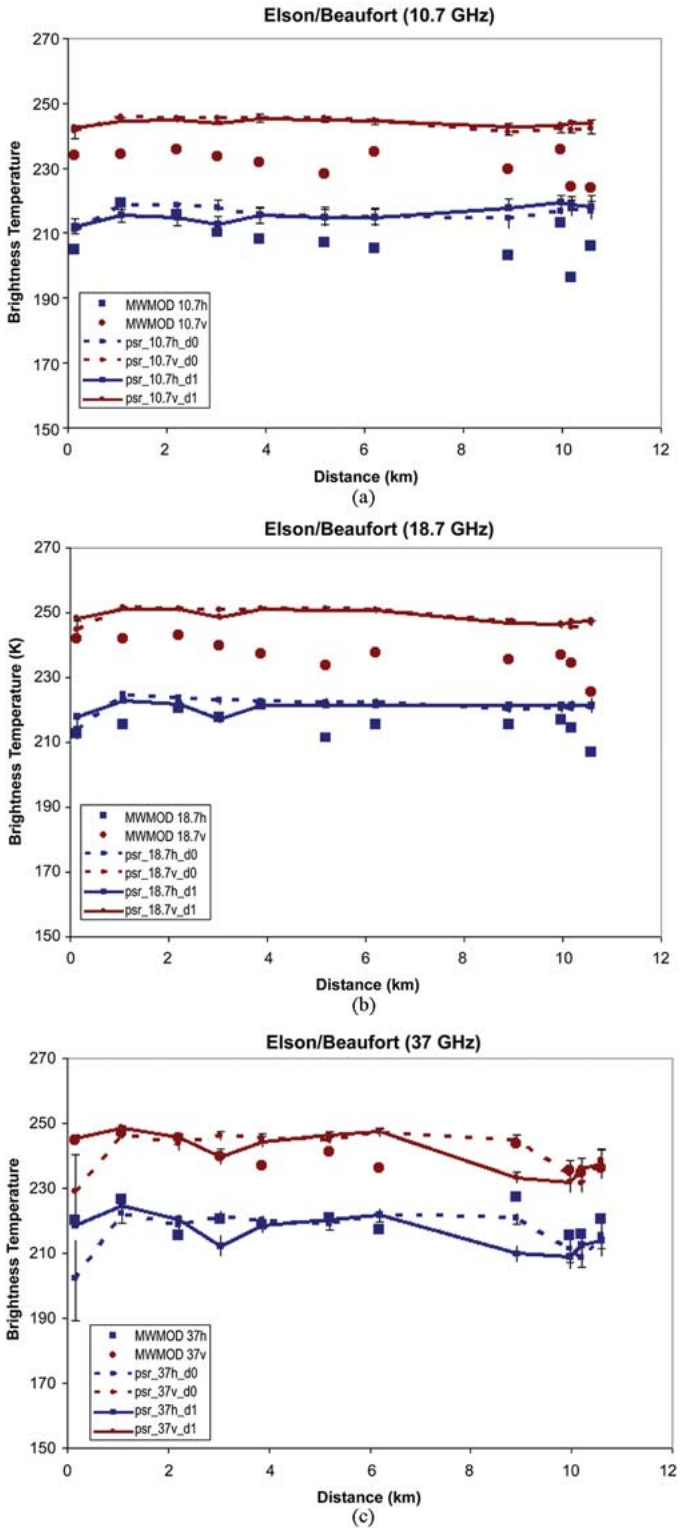

Fig. 7. (a)–(c) Modeled and observed brightness temperatures at each stake location along the Elson Lagoon/Beaufort Sea transect. PSR data are shown for each flight path (solid line = direction d0 and dashed line = direction d1). Horizontal polarizations are shown in blue, and vertical polarizations are shown in red.

For this modeling experiment, values were chosen based on previous measurements of FYI [19]. Ice density was set at $0.92\ \mathrm{g \cdot cm^{-3}}$, and ice bubble diameter and ice grain size were set at 1.2 mm throughout the ice sheet. Salinity is assumed

TABLE II
COMPARISON OF OBSERVED (PSR) AND MODELED (MWMOD) BRIGHTNESS TEMPERATURES AT EACH STAKE LOCATION ALONG THE ELSON LAGOON/BEAUFORT SEA TRANSECT. RESULTS ARE SHOWN FOR BOTH PSR FLIGHT DIRECTIONS (WHITE AND DARK GRAY), WHEREAS THE MODELED VALUES ARE SHOWN IN ITALICS. STANDARD DEVIATIONS OF THE PSR Tbs ARE GIVEN INSIDE PARENTHESES

	10V	10H	19V	19H	37V	37H	89V	89H
Elson 0.15 km	241.31 (1.88)	210.75 (2.64)	244.71 (2.68)	214.11 (3.61)	229.15 (11.47)	201.84 (12.53)	164.24 (19.61)	155.06 (17.34)
	242.49 (0.81)	212.10 (2.55)	248.32 (0.79)	218.16 (1.10)	245.56 (0.92)	218.82 (1.23)	237.38 (2.23)	221.98 (2.07)
	233.90	*204.61*	*242.02*	*212.80*	*244.79*	*220.93*	*240.75*	*218.45*
Elson 1.07 km	245.79 (0.97)	218.72 (1.02)	251.44 (0.45)	224.78 (1.20)	246.50 (1.54)	222.24 (2.79)	189.57 (4.34)	177.64 (4.94)
	244.75 (0.93)	215.57 (2.10)	251.23 (0.74)	223.06 (0.84)	248.60 (0.74)	224.83 (0.95)	234.95 (2.73)	221.94 (3.03)
	234.23	*219.19*	*241.93*	*215.53*	*246.78*	*226.50*	*240.92*	*230.10*
Elson 2.21 km	245.47 (0.80)	217.40 (0.79)	251.15 (0.35)	223.75 (0.88)	243.82 (2.46)	218.88 (3.56)	182.73 (5.37)	171.51 (5.41)
	244.87 (1.03)	214.96 (2.56)	250.97 (0.74)	221.87 (1.00)	245.67 (1.28)	220.39 (1.40)	222.15 (2.74)	209.22 (2.42)
	235.69	*215.60*	*243.00*	*220.64*	*245.30*	*228.95*	*240.54*	*224.10*
Elson 3.03 km	245.47 (0.84)	216.78 (2.65)	250.67 (0.63)	223.04 (1.48)	246.06 (1.40)	221.38 (2.02)	190.53 (6.12)	177.77 (4.48)
	243.94 (0.72)	212.70 (2.70)	248.56 (0.83)	217.43 (1.61)	239.62 (2.50)	212.39 (3.58)	210.84 (4.01)	198.24 (4.18)
	233.54	*210.14*	*239.83*	*217.64*	*239.71*	*215.95*	*237.79*	*218.58*
Elson 3.87	245.29 (0.97)	215.95 (2.79)	250.96 (0.63)	222.78 (1.45)	245.44 (1.42)	220.18 (1.91)	190.64 (5.99)	177.48 (4.39)
	245.36 (1.49)	215.60 (2.30)	251.06 (0.72)	221.74 (1.25)	244.24 (1.82)	218.84 (2.53)	210.99 (4.71)	198.81 (5.43)
	231.80	*207.77*	*237.68*	*221.69*	*236.85*	*218.13*	*238.39*	*219.59*
Elson 5.20 km	245.46 (1.08)	215.80 (3.06)	251.01 (0.71)	222.44 (1.47)	244.82 (1.13)	219.13 (1.68)	195.02 (6.85)	181.45 (6.02)
	244.85 (0.88)	215.08 (2.32)	250.84 (0.63)	221.59 (1.17)	246.46 (1.20)	220.55 (2.34)	216.73 (4.14)	203.61 (4.90)
	228.26	*206.79*	*233.54*	*211.37*	*241.09*	*220.89*	*234.21*	*208.87*
Elson 6.19 km	244.80 (1.21)	215.46 (2.92)	250.73 (0.93)	222.45 (1.52)	247.05 (1.24)	221.85 (1.94)	206.91 (6.68)	193.44 (6.11)
	244.48 (0.84)	215.08 (2.35)	250.81 (0.52)	221.70 (1.08)	247.42 (1.10)	222.10 (1.79)	220.14 (4.75)	206.88 (4.95)
	234.88	*205.08*	*237.65*	*216.18*	*236.01*	*217.39*	*227.77*	*202.45*
Beaufort 8.92 km	241.01 (0.81)	214.49 (0.95)	247.35 (0.76)	220.31 (1.09)	244.57 (1.76)	220.80 (1.76)	217.47 (4.40)	207.16 (4.22)
	242.73 (1.06)	218.02 (2.59)	246.87 (0.70)	221.42 (1.29)	233.27 (1.82)	209.73 (2.88)	185.07 (7.25)	177.711 (7.29)
	229.68	*202.95*	*235.25*	*214.33*	*243.92*	*227.15*	*248.91*	*231.50*
Beaufort 9.97 km	242.00 (0.93)	216.65 (2.40)	245.97 (0.78)	220.33 (1.14)	234.42 (4.12)	211.40 (4.33)	192.26 (11.04)	184.63 (9.91)
	243.14 (0.87)	219.50 (2.11)	246.58 (0.92)	221.74 (1.20)	232.02 (3.17)	208.67 (3.73)	172.77 (12.84)	165.81 (12.74)
	235.02	*211.73*	*236.84*	*216.88*	*237.67*	*217.58*	*247.30*	*224.95*
Beaufort 10.2 km	241.88 (0.93)	217.63 (2.64)	245.43 (0.80)	220.50 (1.24)	231.44 (2.88)	208.46 (2.78)	185.04 (4.21)	178.33 (4.02)
	243.89 (0.89)	218.91 (2.45)	247.37 (0.69)	221.72 (1.68)	236.03 (3.19)	212.69 (4.03)	178.94 (11.58)	170.97 (11.11)
	224.43	*196.07*	*234.36*	*214.44*	*238.56*	*217.07*	*241.80*	*218.69*
Beaufort 10.6 km	242.16 (1.28)	216.85 (3.25)	246.71 (0.81)	220.89 (1.22)	238.53 (3.38)	215.48 (4.03)	202.74 (13.83)	193.43 (11.16)
	244.00 (1.03)	218.11 (3.57)	247.58 (0.97)	221.69 (2.45)	237.64 (4.51)	214.21 (5.52)	182.89 (14.68)	173.01 (11.82)
	223.91	*203.91*	*225.53*	*206.78*	*236.14*	*220.47*	*246.43*	*231.84*

to follow a C-shaped profile with a bulk salinity of 9% for Elson Lagoon (which is a valid assumption for cold March sea ice—surface air temperatures ranged between -30 °F and -20 °F) and mostly linear with a bulk salinity of 5% for the Beaufort Sea. Field data inputs into the model included ice thickness, snow depth, snow density, snow grain size, snow type (e.g., hoar fraction), snow liquid water content, and temperature at the snow surface, snow/ice interface, and 10 cm into the ice. For temperatures at different layers, a linear profile was used. In Fig. 7, we exclude the 89-GHz data since the data exhibited too much scatter to be of any use for this comparison. Nevertheless, we include the mean and standard deviation of the 89-GHz Tbs at the stake locations in Table II. The PSR data are shown for each flight path [e.g., solid line = direction 0 (d0) and dashed line = direction 1 (d1)]. Typically, the Tbs are the same for both flight paths, except at 37 and 89 GHz.

In general, MWMOD accurately simulates the horizontal Tbs. Mean differences between the PSR observations and model results combining both flight paths at 10.7, 18.7, and 37 GHz are 8.1 K ($\pm$6.04 K), 5.9 K ($\pm$4.17 K), and 3.3 K ($\pm$6.17 K), respectively. Note, however, that the fit is sometimes better for one flight path than the other, which may reflect a dependence of the PSR radiances on changes in surface roughness between the two flight paths. There are several instances where the mean PSR Tbs differ by more than 10 K between flight paths and/or where the modeled Tbs are well within the standard deviation of the PSR data.

In general, the fit is slightly better for the Elson Lagoon transect than for the Beaufort Sea. This is not surprising since the surface of Elson Lagoon was relatively smooth compared to the Beaufort Sea, and MWMOD does not explicitly account for roughness. At the Elson Lagoon stakes, mean differences

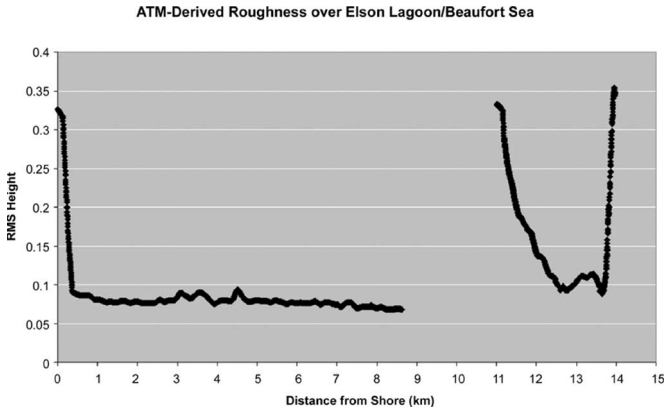

Fig. 8. RMS height variations measured by the ATM along the Elson Lagoon/ Beaufort Sea transect.

at horizontal polarization drop at all frequencies (e.g., 5.3 K at 10.7 GHz, 4.9 K at 18.7 GHz, and 1.1 K at 37 GHz). Given that the standard deviation of the PSR data can be as high as 12 K, these results are well within the accuracy of the PSR data.

Results are significantly worse at vertical polarizations, except at 37 GHz. At 10.7 and 18.7 GHz, MWMOD systematically underestimates the Tbs by 12.4 K ($\pm$4.07 K) and 11.8 K ($\pm$4.59 K), respectively. At 37 GHz, MWMOD is within 1.1 K ($\pm$6.27 K) of the PSR data (and typically within the standard deviation of the PSR measurement). At this frequency, there is essentially no difference in how the model simulations compare with the observations for Elson Lagoon or the Beaufort Sea. However, there is a general decrease in the 37-GHz H- and V-polarized Tbs as the observations move from Elson Lagoon to the Beaufort Sea. This is a result of the deeper snowpack observed for the Beaufort Sea area sampled since at 37 GHz, the emission is nearer the surface. Overall, since the vertically polarized channels are less influenced by surface conditions than the horizontal channels, the differences between the modeled and PSR-observed 10.7- and 18.7-GHz vertically polarized Tbs represent a systematic bias in the model output and/or PSR calibration issues.

B. Impact of Surface Roughness on Tbs

Surface roughness is known to significantly impact microwave emission of the sea ice/snow surface. Details of the types of ice conditions encountered during the AMSR-Ice03 field experiment are discussed in [9] and [18]. Markus *et al.* [9] discuss classifications of ice type and roughness derived from PSR and Airborne Terrain Mapper (ATM) [7] data. Results from this paper show that Elson Lagoon was relatively smooth compared with the more deformed Beaufort sea ice (Fig. 8).

Smooth ice was observed to exhibit similar 18.7 V and 37 V Tbs, whereas rougher ice exhibited higher Tbs at 18.7 V than at 37 V [9]. Overall, however, the mean Tbs for the different ice classes were relatively constant for the vertical polarization channels and varied slightly more for the horizontally polarized channels (see [9]). Since the horizontal channels are more sensitive to surface features, any change in ice or snow properties, including features such as hoar and ice lenses, will affect the Tbs at this polarization.

Although the surface of Elson Lagoon was relatively smooth compared to the more deformed Beaufort sea ice, small-scale surface roughness (i.e., millimeter to meter scale) may still significantly impact the observed PSR Tbs. In addition, the Elson Lagoon transect exhibited some large snow drifts. The impact of these features on the observed Tbs can be seen in Fig. 4(a) where there remains dependence of the PSR Tbs on the aircraft flight direction over Elson Lagoon. However, since there is generally more variability in the PSR Tbs for the Beaufort Sea than Elson Lagoon [Fig. 4(b)], this suggests that roughness indeed contributes to differences in Tbs between flight lines.

Unfortunately, MWMOD does not explicitly include surface roughness as a model parameter. However, one way to evaluate how surface roughness may affect the Tbs is through variation of the sensor incidence angle, which can be set in the MWMOD computations. Modeling the Tbs as a function of incidence angle allows us therefore to examine the effect of roughness independent of snow depth on the Tbs as the "effective" incidence angle changes if the surface is not flat (e.g., examine the influence of the orientation of roughness features). Since the PSR views the surface at about 55°, rough facets may tend to yield lower effective incidence angles or be unobserved by the PSR (due to the facets being angled away from the PSR view and thus have higher effective incidence angles). Thus, a "very rough" ice surface would yield emissions at effective incidence angles that were either very small or very large. A less rough surface would yield emission at incidence angles around 55°. For this reason, in the subsequent model runs, sea ice, snowpack, and atmospheric conditions were kept constant, and only the sensor incidence angle was varied so that it would be possible to investigate how roughness facets may impact the AMSR-E Tbs.

Fig. 6 showed how strongly the Tbs can vary with the incidence angle. Since we do not know the effective incidence angle (i.e., the true angle of the surface elements relative to the PSR), we need to derive it. One way to hypothetically determine the effective incidence angle is by finding the incidence angle at which the modeled polarization ratio (PR) and/or gradient ratio (GR) match most closely with the PR and/or GR computed from the PSR data. The reason for using the PR is because PR differences between MWMOD, and the PSR data agree better than the Tbs, and therefore, the PR may be used to determine the incidence angle at which MWMOD and PSR agree the best. The PR at 18.7 GHz is defined for example as

$$\mathrm{PR} = [\mathrm{Tb}(18.7\,\mathrm{V}) - \mathrm{Tb}(18.7\,\mathrm{H})]/[\mathrm{Tb}(18.7\,\mathrm{V}) + \mathrm{Tb}(18.7\,\mathrm{H})]. \quad (1)$$

The PR is also derived at 10.7 and 37 GHz. The 37/18.7 GR at vertical polarizations is given by

$$\mathrm{GR} = [\mathrm{Tb}(37\,\mathrm{V}) - \mathrm{Tb}(18.7\,\mathrm{V})]/[\mathrm{Tb}(37\,\mathrm{V}) + \mathrm{Tb}(18.7\,\mathrm{V})]. \quad (2)$$

In a physical sense, the PR varies depending on ice conditions, including surface roughness. For example, heavily ridged ice typically contains areas of exposed ice blocks and areas of deep and layered snow within the ridges, which results in a reduction in the horizontally polarized emissivity. In addition, scattering from layered snowpacks that include hoar crystals further acts to reduce the emissivity at horizontal polarizations. Thus, since the horizontally polarized channels are more sensitive to snow and ice characteristics, the depolarization

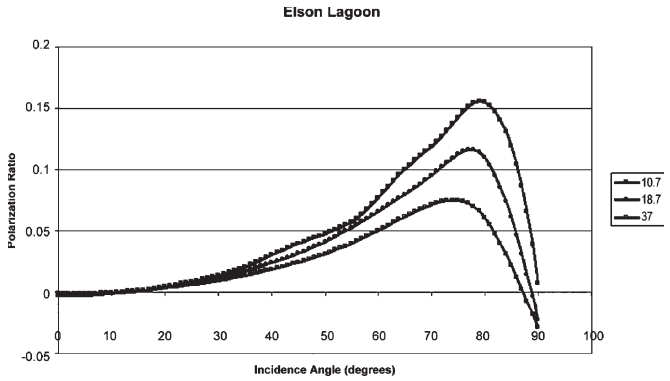

Fig. 9. Dependence of the PR at 10.7, 18.7, and 37 GHz on sensor incidence angle.

(i.e., the PR going toward 0) may indicate an increase in roughness. Comparisons of the PR at different frequencies show that different frequencies correspond to different features in the ice cover [9]. For example, Markus *et al.* [9] show that low PR values at 10.7 GHz correspond to ridged ice, which is likely a result of the greater penetration depth at 10.7 GHz. At 18.7 GHz, these ridged ice areas become less distinct, and at 37 GHz, the emission is mostly influenced by the surface ice features and snow depth. Fig. 9 illustrates the variation of the PR at 10.7, 18.7, and 37 GHz over Elson Lagoon as a function of incidence angle. At low incidence angles (and, hence, rougher surfaces), the PR goes to zero. The decline in PR from 55° to 0° is steepest at 10.7 GHz, which supports the earlier conclusion that the 10.7-GHz PR values relate to rougher ice (i.e., heavily ridged ice).

The GR (37/18.7) also reflects the roughness of the surface, since the Tbs are higher at 18.7 V than at 37 V when the surface is rough. Therefore, the GR will be more strongly negative for rough ice than for smooth ice. The GR is important in the suite of AMSR-E sea ice products since it is used to retrieve snow depths by using the knowledge that the GR becomes more negative as snow depth increases (e.g., 37 V Tbs decrease), whereas with no snow, the GR is approximately zero. Thus, because the GR is also sensitive to snow depth, it is not possible to separate out the effects of changes in surface roughness from those resulting from changes in snow depth.

Table III lists the effective incidence angle (which is defined as the angle with the smallest PR and GR differences between simulated values of the PR and GR and those obtained from the PSR observations) together with the value of the PR and GR at the returned effective incidence angle from MWMOD and the mean PSR PR and GR (together with the standard deviation). According to [9], the PR at 10.7 GHz is higher for smooth ice than for ridged or rubbled ice (see [9, Table 3]). This statement appears to hold true, as we can see a clear shift in ice type between the transect that covers the Beaufort Sea and the one that covers Elson Lagoon by the change in PR10.7. This shift also coincides with a shift toward smaller effective incidence angles and suggests that the roughness elements in the Beaufort Sea were oriented toward the PSR view. At stake 0.15 km, a relatively small effective incidence angle was also returned over Elson Lagoon. According to ATM transects, this area along the Elson transect exhibited large rms height variations compared to the rest of the Elson line (e.g., see Fig. 8 and Table III).

TABLE III
RETRIEVED EFFECTIVE INCIDENCE ANGLE (IN BOLD TYPE) USING DIFFERENT PRS AND GRS. SHOWN ARE THE EFFECTIVE INCIDENCE ANGLE RETRIEVED TOGETHER WITH THE MWMOD PR AND GR AT THE EFFECTIVE INCIDENCE ANGLE AND THE PSR MEAN PR AND GR WITH STANDARD DEVIATIONS GIVEN INSIDE PARENTHESES. MEAN SNOW DEPTH, ICE THICKNESS, AND ATM RMS HEIGHT SURROUNDING THE STAKE LOCATIONS ARE ALSO SHOWN FOR COMPARISON

Stake Location (km)	PR10.7 Angle (degrees) (MWMOD/ PSR)	PR18.7 Angle (degrees) (MWMOD/ PSR)	PR37 Angle (degrees) (MWMOD/ PSR)	GR37/18.7 Angle (degrees) (MWMOD/ PSR)	Mean Snow Depth (cm)	Mean Ice Thickness (m)	ATM RMS Height
Elson 0.15	**41** 0.0683 0.0672 (0.0049)	**52** 0.0665 0.0656 (0.0027)	**58** 0.0597 0.0606 (0.0057)	**60** -0.0002 -0.0193 (0.0196)	8.4		0.327
Elson 1.07	**43** 0.0608 0.0605 (0.0039)	**57** 0.0579 0.0574 (0.0026)	**64** 0.0511 0.0511 (0.0031)	**52** 0.0019 -0.0079 (0.0033)	14.1		0.081
Elson 2.21	**48** 0.0627 0.0628 (0.0041)	**56** 0.0606 0.0596 (0.0025)	**64** 0.0537 0.0541 (0.0030)	**56** -0.0026 -0.0128 (0.0043)	17.3	1.6	0.076
Elson 3.03	**50** 0.0655 0.0647 (0.0066)	**56** 0.0624 0.0618 (0.0049)	**81** 0.0552 0.0559 (0.0052)	**4** -0.0130 -0.0130 (0.0054)	8.3	2.2	0.082
Elson 3.87	**49** 0.0633 0.0641 (0.0047)	**55** 0.0611 0.0606 (0.0025)	**61** 0.0544 0.0545 (0.0026)	**61** -0.0123 -0.0123 (0.0036)	17.0	1.9	0.079
Elson 5.20	**58** 0.0647 0.0645 (0.0053)	**90** 0.0597 0.0610 (0.0022)	**56** 0.0546 0.0554 (0.0028)	**17** -0.0113 -0.0111 (0.0031)	17.9	1.8	0.079
Elson 6.19	**49** 0.0648 0.0639 (0.0053)	**51** 0.0609 0.0605 (0.0022)	**62** 0.0535 0.0538 (0.0032)	**74** -0.0068 -0.0072 (0.0024)	16.2		0.076
Beaufort 8.92	**42** 0.0551 0.0557 (0.0047)	**50** 0.0564 0.0559 (0.0025)	**62** 0.0516 0.0522 (0.0040)	**59** 0.0061 -0.0181 (0.0118)	3.9	1.6	
Beaufort 9.97	**36** 0.0528 0.0533 (0.0049)	**44** 0.0536 0.0541 (0.0021)	**58** 0.0530 0.0523 (0.0036)	**51** -0.0162 -0.0271 (0.0078)	13.3	2.7	
Beaufort 10.2	**39** 0.0535 0.0534 (0.0054)	**52** 0.0543 0.0541 (0.0025)	**56** 0.0521 0.0521 (0.0045)	**60** 0.0074 -0.0266 (0.0067)	22.6	2.6	0.331
Beaufort 10.6	**42** 0.0559 0.0556 (0.0067)	**46** 0.0554 0.0552 (0.0036)	**65** 0.0519 0.0512 (0.0062)	**59** 0.0029 -0.0184 (0.0089)	18.6	1.9	0.192

The shift toward smaller effective incidence angles for the Beaufort transect is also apparent in PR18.7, since at 18.7 GHz, the PR remains sensitive to rougher ice, although the sensitivity is reduced compared with that observed at 10.7 GHz. At 37 GHz, however, this shift is not observed. This is not surprising since at 37 GHz, snow depth dominates the emission at 37 GHz, and thus, PR37 is responding to both changes in the orientation of surface features as well as changes in snow depth. Snow depth was highly variable over both Elson Lagoon and the Beaufort Sea, with deeper drifts observed along the Beaufort transect (e.g., Fig. 2). Thus, locations where rougher ice was observed were also locations where the deepest snow was found. Since 37 V would decrease with a deeper snowpack, the GR should become more strongly negative, which is exactly what was observed in the PSR GR. In Table III, the mean snow depth and ice thickness between 100 m from the stakes are also listed and show that, in general, the deeper the snowpack, the more negative the GR.

Since observations at 10.7 GHz appear to respond to ridged ice areas because of the greater penetration depth at that frequency, and because the roughness features are tilted toward the view of the PSR (which is seen in the lower effective incidence angles as we move toward rougher surfaces), we should theoretically see a relationship between the effective incidence angle and the standard deviation of ice thickness (a proxy for roughness). In Fig. 3, ice thickness from electromagnetic

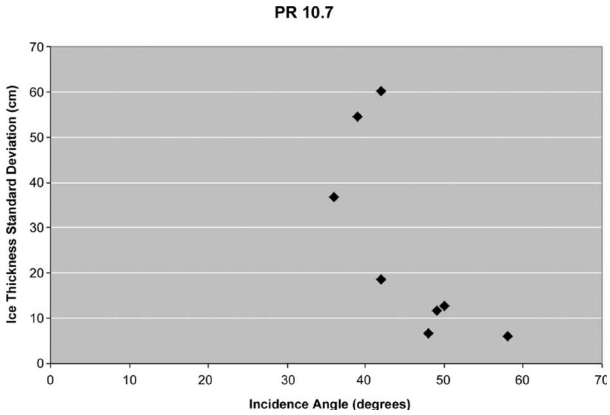

Fig. 10. Effective incidence angle retrieved using PR10.7 as a function of the standard deviation of ice thickness.

(EM-31) observations are shown, although there are large gaps where no observations were made. Some estimates of the variability of the ice thickness for the Beaufort stake locations are given in [18]. Here, we use the data shown in Fig. 3 to compute the standard deviations of ice thickness within 100 m of the stake location and compare those with the effective incidence angle derived from PR10.7. Results are shown in Fig. 10 for all stakes, except at 0.15, 1.07, and 6.19 km where no data on ice thickness are available. In general, the smallest standard deviations occur at higher effective incidence angles, suggesting that the surface features are relatively flat (e.g., smooth ice). At higher standard deviations, the effective incidence angle tends to be smaller but becomes somewhat unambiguous for large rubbled ice (i.e., like that found at stake 10.6 km). Since roughness features can take on any orientation, the effective incidence angle is not necessarily less than the PSR viewing angle—it may also be possible that the roughness facets are angled away from the PSR.

C. Impact of Surface Roughness on Derived Sea Ice Concentration and Snow Depth

This section examines how roughness affects retrievals of sea ice concentration and snow depth from the NT and NT2 sea ice algorithms. Fig. 11 summarizes ice concentration results for Elson stake locations as a function of incidence angle, whereas Fig. 12 shows results at the Beaufort Sea stakes. After an incidence angle of around 40°, both the NT and NT2 algorithms begin to return less than 100% ice fraction and after about 80°, the ice concentration falls to 0%. Thus, after about 80°, the facets are angled completely away from the sensor view and are therefore not observed. The decline is steeper for the NT algorithm than for the NT2 algorithm, suggesting greater sensitivity of the NT algorithm to roughness features. Table IV summarizes algorithm retrieved sea ice concentrations assuming an incidence angle of 55° and also assuming an effective incidence angle as derived by minimizing the modeled and observed PRs/GRs. It is clear that if the surface is assumed to be completely flat, the NT and NT2 sea ice algorithms underestimate the total ice concentration, with greater reductions for the NT algorithm. It is important to remember, however, that PSR calibration issues may affect the returned sea ice concentrations shown in Table IV, particularly for the NT2 algorithm since

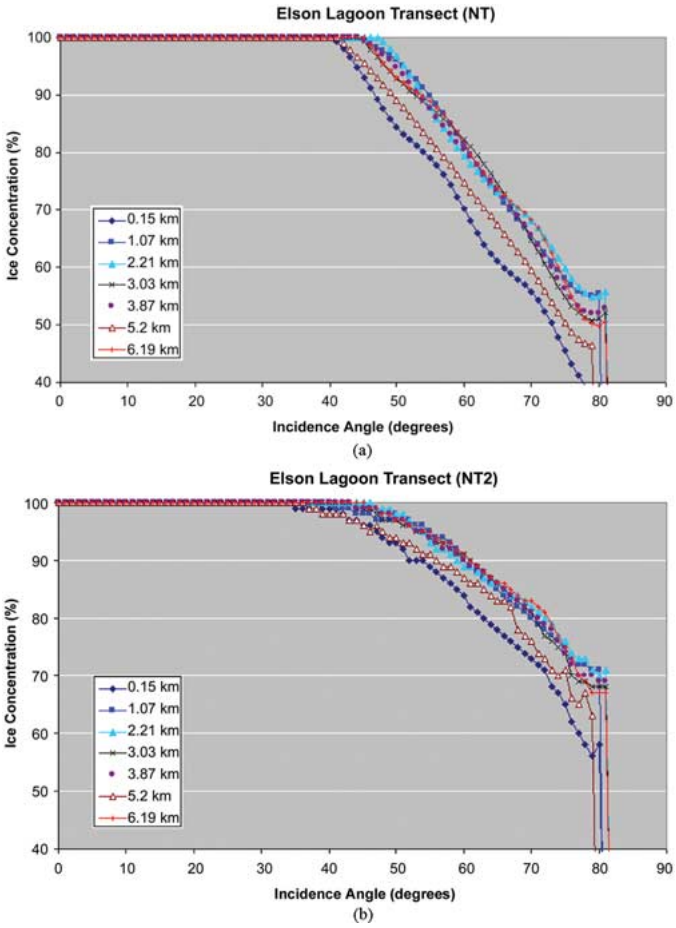

Fig. 11. (a) Sea ice concentration as a function of incidence angle along the Elson Lagoon transect for the NT sea ice algorithm. (b) Sea ice concentration as a function of incidence angle along the Elson Lagoon transect for the NT2 sea ice algorithm.

it uses the 89-GHz channels, which could not be adequately calibrated toward AMSR-E.

Ice concentrations depend on the effective incidence angle because both algorithms use the PR to derive ice concentration. Therefore, the effects of roughness on the PR will translate into errors in ice concentration. If, for example, the PR at 10.7 were to be used as a proxy of surface roughness, improved estimates of total ice concentration would result. At the effective incidence angles derived using PR10.7, the mean error in ice concentration for Elson Lagoon is 4.7% for the NT algorithm and 2.6% for the NT2 algorithm. For the area of the Beaufort Sea sampled, the error is 0.2% and 1.7% for the NT and NT2 algorithm, respectively. However, if we assume a completely flat surface, both algorithms underestimate the total ice concentration by 13.9% for the NT algorithm and 7.2% for the NT2 algorithm. These underestimations in total ice concentration may be different if the area sampled also included open-water areas and may also result in overestimation of the ice fraction. For all the stake locations evaluated, the effective incidence angle computed from PR10.7 gives an NT-derived mean ice concentration of 96.9% and an NT2-derived ice concentration of 97.5%. Furthermore, it can be seen that the rougher ice locations have ice concentrations closer to 100% when we use the effective incidence angle derived from PR10.7.

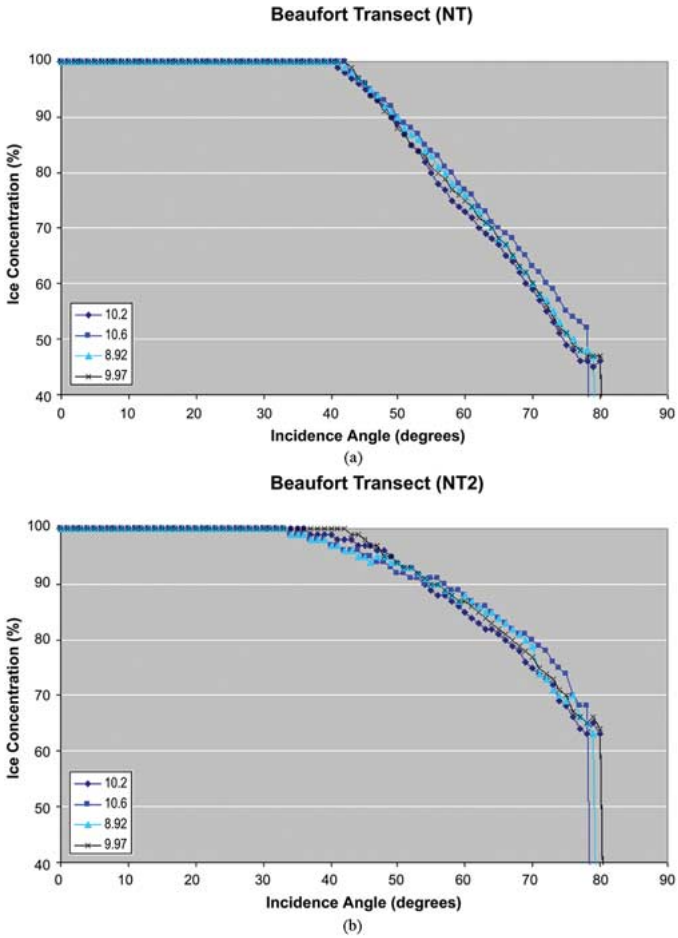

Fig. 12. (a) Sea ice concentration as a function of incidence angle along the Beaufort Sea transect for the NT sea ice algorithm. (b) Sea ice concentration as a function of incidence angle along the Beaufort Sea transect for the NT2 sea ice algorithm.

TABLE IV
SEA ICE CONCENTRATION IN PERCENT FOR THE NT AND NT2 SEA ICE ALGORITHMS FOR THE PSR INCIDENCE ANGLE AND EFFECTIVE INCIDENCE ANGLES DERIVED THROUGH COMPARISONS OF MODELED AND OBSERVED PRS AND GRS

Stake Location (km)	55° NT/NT2	PR10.7 Angle NT/NT2	PR18.7 Angle NT/NT2	PR37 Angle NT/NT2	GR Angle NT/NT2
0.15	79/89	99/99	85/93	74/86	70/84
1.07	90/95	100/99	87/94	74/86	94/97
2.21	88/93	100/100	86/92	74/86	86/92
3.03	88/94	95/95	89/95	51/68	100/100
3.87	88/94	98/99	91/95	81/91	81/91
5.20	82/91	81/90	0/0	84/91	100/100
6.19	89/95	94/98	91/96	78/89	60/77
8.92	83/91	100/99	90/94	77/88	81/90
9.97	88/95	100/100	98/97	87/94	89/94
10.2	89/94	100/98	89/95	89/95	78/90
10.6	83/89	99/96	93/94	69/84	81/90

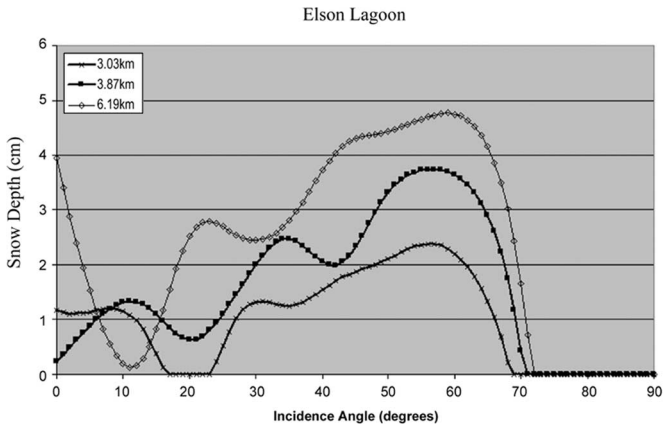

Fig. 13. Snow depth as a function of incidence angle at three stake locations along the Elson Lagoon transect.

Since the AMSR-E sea ice algorithms also include the retrieval of snow depth over seasonal ice, we included evaluation of how well snow depths derived from modeled Tbs matched the observed snow depths. Results indicated that snow depth was not retrieved very well using the MWMOD modeled Tbs. Snow depth is calculated using GR37/18.7 [e.g., (2)]. However, since MWMOD tends to underpredict the Tbs at 18.7 V, this will cause the GR to be more positive than it should be. Adding an offset to the modeled 18.7 V Tbs to better match the PSR observations did not improve the results. This suggests that the AMSR-E snow depth retrieval algorithm is extremely sensitive to the accuracy of instrument calibration. Fig. 13 shows modeled snow depth as a function of incidence angle at the three stake locations along Elson Lagoon where a snow depth greater than 0 cm was returned using the modeled Tbs. It is apparent that the snow depth fluctuates considerably as the incidence angle changes, suggesting that surface roughness has a large impact on the accuracy of snow depth retrievals using the Markus and Cavalieri [11] algorithm. However, at all three stake locations, the measured snow depth was above 10 cm, and therefore, the modeled Tbs were not able to accurately simulate the *in situ* measured snow depth. Further work is needed to investigate the shortcomings of the ability to accurately retrieve snow depths using modeled Tbs and how surface roughness may impact retrieved snow depth using the current algorithm that relies on GR37/18.7.

IV. CONCLUSION

This paper uses an RTM approach to simulate Tbs over sea ice near Barrow, AK, obtained from PSR aircraft observations and investigates the impact of Tbs and subsequently derived sea ice concentrations and snow depth on surface roughness. For this analysis, a combined ocean/sea ice/atmospheric model (MWMOD) is used to simulate AMSR-E Tbs over Elson Lagoon and the Beaufort Sea. The first analysis focused on determining the ability of MWMOD to simulate the observed Tbs. Results showed that, in general, MWMOD is able to accurately simulate Tbs over the FYI examined in this paper. Results are better at horizontal polarizations than at vertical ones, but given the uncertainties in the calibration of the PSR Tbs, it remains unclear if the differences between observed and modeled Tbs are a result of the inability of the model to accurately simulate the vertical polarizations, especially at lower frequencies. At 37 GHz, MWMOD output matches observations to within about 1 K. We were not able to evaluate the sensitivity of the 89-GHz channel to sea ice properties because of calibration

issues. This was unfortunate, since the 89-GHz channel plays a central role in the AMSR-E sea ice algorithm (e.g., NT2).

Comparisons between modeled PRs at 10.7 GHz with those from the PSR confirm that the PR decreases as the surface becomes more ridged/rubbled. It is apparent that passive microwave Tbs are very sensitive to the orientation of the surface elements relative to the sensor viewing angle, which, in turn, can result in different retrievals of ice concentration and snow depth from sea ice algorithms. In this paper, the roughness facets appear to be oriented toward the PSR and therefore yield emissions at angles less than 55°. For example, at the Beaufort Sea stake locations, we found a reduction in the "effective" incidence angle over the Beaufort Sea compared with Elson Lagoon. The smoother surface of Elson Lagoon exhibited gradual slopes on the order of 5°–10°, whereas the rougher Beaufort Sea showed slopes on the order of 13°–20°. ATM rms height estimates as well as standard deviation of ice thickness around the stake locations confirm the relationship between the PR at 10.7 and the changes in the effective incidence angle and the roughness of the surface. A relationship is also observed at 18.7 GHz, but not as strong as at 10.7 GHz, which suggests that the PR at 10.7 GHz can provide good estimates of areas of ridged and heavily rubbled ice. At 37 GHz, snow masks the underlying ice roughness, and therefore, PR37 is not a useful measure of surface roughness as indicated by the decrease in correlation between roughness and PR37 in Table III. Results here are in agreement with the results presented in [9].

The orientation of the roughness facets relative to the sensor strongly influences the Tbs and therefore the sea ice concentration returned by the NT2 and NT sea ice algorithms. The dependence of algorithm performance on incidence angle is less for the NT2 algorithm than for the NT algorithm, but both algorithms can significantly underestimate the fraction of sea ice if the effective incidence angle is unknown. If we assume a flat surface and a constant PSR incidence angle of 55°, the amount of sea ice can be underestimated by more than 20% for the sea ice areas sampled in this paper. Using the effective incidence angle derived through comparisons of PR10.7 results in ice concentrations typically within a couple percent of those observed, except at stake location 5.20 km.

Results here also confirm that the Tbs are sensitive to small variations in incidence angles near 50° such as those induced by changing from the SMMR to SSM/I, and AMSR instruments could induce differences in ice concentration estimates on the order of 5%–10%. This is not a factor typically considered when combining sea ice concentration data sets that span several satellite sensors, and depending on the amount of open water present, the differences could be greater. However, it is important to keep in mind that over the larger satellite footprint, these features may be "smoothed" out. This needs to be investigated in more detail.

GR37/18.7 is used to determine snow depth in the AMSR-E sea ice algorithm. Results here show that the correlation between GR37/18.7 and snow depth was higher (and positive) for the Elson Lagoon stakes than for the Beaufort Sea stake locations (e.g., −0.57 versus −0.48). On the other hand, there is a strong correlation between GR37/18.7 and surface roughness (−0.81), where a rougher surface causes a decrease in GR37/18.7. Thus, to improve snow depth retrievals from AMSR-E using GR37/18.7, information on surface roughness could potentially improve snow depth retrievals, such as using different slopes depending on the roughness characteristics of the underlying sea ice.

Overall, this paper demonstrates the importance of ridged and rubbled ice on passive microwave Tbs as well as the sea ice concentrations and snow depth derived from these Tbs. The effects of roughness will cause errors in retrieved ice concentration for both of the current NT sea ice algorithms. The use of PR10.7 to identify roughness facets could potentially lead to improved estimates in both sea ice concentration and snow depth retrievals from AMSR-E. However, we caution that many more observations of surface roughness and snow depth, particularly for different ice types and at larger spatial scales are needed to further test the conclusions reached in this paper and to evaluate the impact that roughness would have on satellite-derived products. This is the goal of the AMSR-Ice06 field campaign during March 2006, which will extend the data collection made in 2003 by mapping snow depth and surface roughness over larger areas rather than along long traverse lines.

ACKNOWLEDGMENT

The authors would like to thank all the members involved in the AMSR-Ice03 field campaign, including the field and aircraft crew members and the logistical support from the Barrow Arctic Science Consortium.

REFERENCES

[1] D. J. Cavalieri, T. Markus, J. A. Maslanik, M. Sturm, and E. Lobl, "March 2003 EOS Aqua AMSR-E Arctic sea ice field campaign," *IEEE Trans. Geosci. Remote Sens.*, vol. 44, no. 11, pp. 3003–3008, Nov. 2006.

[2] D. J. Cavalieri, C. L. Parkinson, P. Gloersen, and H. J. Zwally, "Arctic and Antarctic sea ice concentrations, from multichannel passive-microwave satellite data sets: October 1978 to September 1995, User's Guide," NASA Goddard Space Flight Center, Greenbelt, MD, NASA Tech. Memo. 104627, 1997.

[3] D. J. Cavalieri and P. Gloersen, "Determination of sea ice parameters with the Nimbus 7 SMMR," *J. Geophys. Res.*, vol. 89, no. D4, pp. 5355–5369, 1984.

[4] J. C. Comiso, "Characteristics of Arctic winter sea ice from satellite multispectral microwave observations," *J. Geophys. Res.*, vol. 91, no. C1, pp. 975–994, 1986.

[5] D. T. Eppler *et al.*, "Passive microwave signatures of sea ice," in *Microwave Remote Sensing of Sea Ice*, ser. Geophysical Monograph, vol. 68, F. D. Carsey, Ed. Washington, DC: Amer. Geophys. Union, 1992, ch. 4, pp. 47–71.

[6] R. Fuhrhop, C. Simmer, M. Schrader, G. Heygster, K.-P. Johnsen, and P. Schussel, "Study of passive remote sensing of the atmosphere and the surface ice," Executive Summary and Final Report, ESA, Noordwijk, The Netherlands, 1997. ESA ESTEC Contract 11198/94/NL/CN.

[7] W. R. Krabill, R. H. Thomas, C. F. Martin, R. N. Swift, and E. B. Frederick, "Accuracy of airborne laser altimetry over the Greenland ice sheet," *Int. J. Remote Sens.*, vol. 16, no. 7, pp. 1211–1222, 1995.

[8] H. J. Liebe, P. W. Rosenkranz, and G. A. Hufford, "Atmospheric 60-GHz oxygen spectrum: New laboratory measurements and line parameters," *J. Quant. Spectrosc. Radiat. Transf.*, vol. 48, no. 5/6, pp. 629–643, 1992.

[9] T. Markus, D. J. Cavalieri, A. J. Gasiewski, M. Klein, J. A. Maslanik, D. C. Powell, B. B. Stankov, J. C. Stroeve, and M. Sturm, "Microwave signatures of snow on sea ice: Observations," *IEEE Trans. Geosci. Remote Sens.*, vol. 44, no. 11, pp. 3081–3090, Nov. 2006.

[10] T. Markus and D. J. Cavalieri, "An enhancement of the NASA team sea ice algorithm," *IEEE Trans. Geosci. Remote Sens.*, vol. 38, no. 3, pp. 1387–1398, May 2000.

[11] ——, "Snow depth distribution over sea ice in the Southern Ocean from satellite passive microwave data," in *Antarctic Sea Ice Physical Processes, Interactions and Variability*, ser. Antarctic Research Series, vol. 74, M. O. Jeffries, Ed. Washington, DC: AGU, 1998, pp. 19–40.

[12] D. C. Powell, T. Markus, D. J. Cavalieri, A. Gasiewski, M. Klein, J. Maslanik, J. Stroeve, and M. Sturm, "AMSR-Ice03 microwave signatures of snow on sea ice: Modeling," *IEEE Trans. Geosci. Remote Sens.*, vol. 44, no. 11, pp. 3091–3102, Nov. 2006.
[13] D. M. Smith, "Extraction of winter total sea-ice concentration in the Greenland and Barents Seas from SSM/I data," *Int. J. Rem. Sens.*, vol. 17, no. 33, pp. 2625–2646, 1996.
[14] A. Stogryn, "A study of the microwave brightness temperature of snow from the point of strong fluctuation theory," *IEEE Trans. Geosci. Remote Sens.*, vol. GE-24, no. 2, pp. 220–231, Mar. 1986.
[15] ——, "Strong fluctuation theory for moist granular media," *IEEE Trans. Geosci. Remote Sens.*, vol. GE-23, no. 1, pp. 78–83, Jan. 1987.
[16] J. C. Stroeve, M. C. Serreze, F. Fetterer, T. Arbetter, W. Meier, J. Maslanik, and K. Knowles, "Tracking the Arctic's shrinking ice cover: Another extreme September minimum in 2004," *Geophys. Res. Lett.*, vol. 32, no. 4, L04501, 2005.
[17] J. C. Stroeve, L. Xiaoming, and J. Maslanik, "An intercomparison of DMSP F11 and F13-derived sea ice products," *Remote Sens. Environ.*, vol. 64, no. 2, pp. 132–152, May 1998.
[18] M. Sturm, J. A. Maslanik, D. K. Perovich, J. C. Stroeve, J. Richter-Menge, T. Markus, J. Holmgren, J. F. Heinrichs, and K. Tape, "Snow and ice measurements from the Beaufort and Chukchi Seas collected during the AMSR-Ice03 campaign," *IEEE Trans. Geosci. Remote Sens.*, vol. 44, no. 11, pp. 3009–3020, Nov. 2006.
[19] W. B. Tucker, D. K. Perovich, A. J. Gow, W. Weeks, and M. R. Drinkwater, "Physical properties of sea ice relevant to remote sensing," in *Microwave Remote Sensing of Sea Ice*, ser. Geophysical Monograph, vol. 68, F. D. Carsey, Ed. Washington, DC: American Geophysical Union, 1992, ch. 2, pp. 9–26.
[20] D. P. Weinbernner *et al.*, "Microwave sea ice signature modeling," in *Microwave Remote Sensing of Sea Ice*, ser. Geophysical Monograph, vol. 68, F. D. Carsey, Ed. Washington, DC: American Geophysical Union, 1992, ch. 8, pp. 137–175.
[21] A. Wiesmann and C. Maetzler, "Microwave emission model of layered snowpacks," *Remote Sens. Environ.*, vol. 70, no. 3, pp. 307–316, Dec. 1999.

Julienne C. Stroeve received the B.S. and M.S. degrees in aerospace engineering and the Ph.D. degree in geography from the University of Colorado, Boulder, in 1989, 1991, and 1996, respectively, where she focused on surface energy balance studies of the Greenland ice sheet using satellite imagery.

Since 1996, she has been with the National Snow and Ice Data Center, Cooperative Institute for Research in Environmental Sciences, University of Colorado, Boulder, as a Research Scientist, specializing in remote sensing of snow and ice. She has extensive experience in remote sensing of the polar regions using satellite imagery that spans the optical to the microwave spectral region. She has participated in several field campaigns in Greenland and the Arctic for the purpose of validation of various geophysical parameters retrieved from spacecraft such as sea ice concentration, surface temperature, and surface reflectivity. Additional research projects include monitoring the rapid decline in ice cover in the Arctic and increased melt of the Greenland ice sheet. At NSIDC, she is responsible for the sea ice products derived from satellite passive microwave data, which includes aiding in the design of Web pages providing general sea ice information and data sets regarding the state of sea ice that may be useful to a broad audience.

Dr. Stroeve is a member of the IEEE Geoscience and Remote Sensing Society, the American Geophysical Union, and the Association of American Geographers.

Thorsten Markus (M'05) received the M.S. and Ph.D. degrees in physics from the University of Bremen, Bremen, Germany, in 1992 and 1995, respectively.

He is currently a Research Scientist with the NASA Goddard Space Flight Center (GSFC), Greenbelt, MD. From 1995 to 1996, he was a National Research Council Resident Research Associate with GSFC before joining NASA-UMBC Joint Center for Earth Systems Technology, where he worked until 2002. His research interests include satellite microwave remote sensing of primarily ice and the utilization of satellite data to study oceanic and atmospheric processes.

Dr. Markus is a member of the American Geophysical Union.

James A. Maslanik received the B.S. degree in forest science and the M.S. degree in environmental pollution control from the Pennsylvania State University, University Park, PA, in 1980 and 1978, respectively, and the Ph.D. degree in geography from the University of Colorado, Boulder, in 1984.

He is a Research Professor with the Department of Aerospace Engineering Sciences, University of Colorado. His research interests include the interactions of sea ice with atmosphere and ocean, remote sensing and field investigations of sea-ice properties, effects of climate change on Arctic coastal communities, and development and deployment of unpiloted aerial vehicles for polar research.

Donald J. Cavalieri (M'05) received the B.S. degree in physics from the City College of New York, New York, in 1960, the M.A. degree in physics from Queens College, New York, in 1967, and the Ph.D. degree in meteorology and oceanography from New York University, New York, in 1974.

From 1974 to 1976, he was a National Research Council Postdoctoral Resident Research Associate with the National Oceanic and Atmospheric Administration's (NOAA) Environmental Data Service, Boulder, CO, where he continued his doctoral research on stratospheric–ionospheric coupling. From 1976 to 1977, he was a Visiting Assistant Professor with the Department of Physics and Atmospheric Science, Drexel University, Philadelphia, PA, where he worked on stratospheric temperature retrievals from satellite infrared radiometers. In the fall of 1977, he was a Staff Scientist with Systems and Applied Sciences Corporation, Riverdale, MD, working on sea ice retrieval algorithms, in preparation for the launch of Nimbus-7 SMMR. In 1979, he joined the Laboratory for Atmospheres, NASA Goddard Space Flight Center, Greenbelt, MD, where he is currently a Senior Research Scientist in the Cryospheric Sciences Branch of the Hydrospheric and Biospheric Sciences Laboratory. His current research interests include polar ocean processes and microwave remote sensing of the cryosphere.

Dr. Cavalieri is a member of the American Geophysical Union and the American Meteorological Society.

Albin J. Gasiewski (S'81–M'88–SM'95–F'02) received the B.S. and M.S. degrees in electrical engineering and the B.S. degree in mathematics from Case Western Reserve University, Cleveland, OH, in 1983, and the Ph.D. degree in electrical engineering and computer science from the Massachusetts Institute of Technology, Cambridge, in 1989.

He is a Professor of electrical and computer engineering with the University of Colorado at Boulder and the Director of the CU Center for Environmental Technology. From 1989 to 1997, he was a Faculty Member with the School of Electrical and Computer Engineering at the Georgia Institute of Technology, where he became an Associate Professor. From 1997 to 2005, he was with the U.S. National Oceanic and Atmospheric Administration's (NOAA) Environmental Technology Laboratory in Boulder, CO, where he was the Chief of the ETL's Microwave Systems Development Division. He has developed and taught courses on electromagnetics, remote sensing, instrumentation, and wave propagation theory. His technical interests include passive and active remote sensing, radiative transfer, antennas and microwave circuits, electronic instrumentation, meteorology, and oceanography.

Prof. Gasiewski is the Past President (2004–2005) of the IEEE Geoscience and Remote Sensing Society. He is a member of the American Meteorological Society, the American Geophysical Union, the International Union of Radio Scientists (URSI), Tau Beta Pi, and Sigma Xi. He currently serves as Vice Chair of USNC/URSI Commission F. He served on the U.S. National Research Council's Committee on Radio Frequencies (CORF) from 1989–1995. He is the General Cochair of IGARSS 2006, to be held in Denver, CO.

John F. Heinrichs (M'06) received the B.S. and M.S. degrees in mathematics from the University of Wisconsin–Milwaukee (UWM), Milwaukee, in 1983 and 1985, respectively, and the Ph.D. degree in geography from the University of Colorado, Boulder, in 1996.

He was a Staff Scientist with the Hughes Aircraft Company from 1986 to 1992, a Research Assistant with the Cooperative Institute for Research in Environmental Sciences (CIRES), Boulder, from 1992 to 1996, and a Postdoctoral Researcher with CIRES from 1996 to 1998. Since 1998, he has been with the faculty of Fort Hays State University, Hays, KS, where he is currently an Associate Professor and the Chair of the Department of Geosciences.

Dr. Heinrichs is a member of the IEEE Geoscience and Remote Sensing Society, the American Geophysical Union, and the Association of American Geographers.

Jon Holmgren received the B.S. degree in geology/geophysics from the University of Alaska–Fairbanks, Fairbanks, in 1987.

He is a Research Scientist with the U.S. Army Cold Regions Research and Engineering Laboratory-Alaska, Ft. Wainwright, where he develops instrumentation and apparatus for field and experimental projects, and operates a commercial machine shop. He has extensive experience in making measurements on sea ice.

Donald K. Perovich received the M.S. and Ph.D. degrees in geophysics from the University of Washington, Seattle, in 1979 and 1983, respectively.

He is currently a Research Geophysicist with the Snow and Ice Branch, U.S. Army Cold Regions Research and Engineering Laboratory, Hanover, NH. He has conducted wide-ranging studies on sea ice, with special focus on optical properties and radiative transfer in sea ice. He was the Chief Scientist for the SHEBA Project, an experiment where a ship was frozen into the Arctic pack and allowed to drift for a year.

Dr. Perovich is a member of the American Geophysical Union, the International Glaciological Society, the American Meteorological Society, and the Electromagnetics Academy.

Matthew Sturm received the M.S. and Ph.D. degrees in geophysics from the University of Alaska, Fairbanks, AK, in 1984 and 1989, respectively.

He is currently a Research Scientist with the U.S. Army Cold Regions Research and Engineering Laboratory-Alaska, Fort Wainwright, AK. He has led over 15 Arctic expeditions. His research interests include Arctic climate change, snow on land, and snow on sea ice.

Dr. Sturm is a member of the American Geophysical Union, the International Glaciological Society, and the Arctic Institute of North America.